# Understanding Förster energy transfer through the lens of molecular dynamics

Mattia Anzola,[†] Cristina Sissa,[†] Anna Painelli,[*,†] A. Hassanali,[‡] and Luca Grisanti[*,¶]

[†]*Department of Chemistry, Life Science and Environmental Sustainability, Parma University, Parco Area delle Scienze 17/A, 43124 Parma, Italy*

[‡]*Condensed Matter and Statistical Physics, International Centre for Theoretical Physics, Strada Costiera 11, Trieste 34151 Italy*

[¶]*Division of Theoretical Physics, Ruđer Bošković Institute, Bijenička cesta 54, 10000 Zagreb, Croatia*

E-mail: anna.painelli@unipr.it; lgrisant@irb.hr

**Abstract**

A multiscale approach to the dynamics of resonant energy transfer is presented, combining DFT and TD-DFT results on the energy donor ($D$) and acceptor ($A$) moieties with an extensive equilibrium and non-equilibrium molecular dynamics (MD) analysis of a bound D-A pair in solution to build a coarse-grained kinetic model. We demonstrate that a thorough MD study is needed to properly address RET: the enormous configuration space visited by the system cannot be reliably sampled accounting only for a few representative configurations. Moreover, the conformational motion of the RET pair, occurring in a similar timescale as the RET process itself, leads to a sizable increase of the overall process efficiency.

# 1 Introduction

Resonance energy transfer (RET) describes a process where energy is transferred from an excited molecule, called the energy donor, to an acceptor molecule, in a process:

$$D^*A \rightarrow DA^* \tag{1}$$

where the star indicates an excited state of the energy donor $D$ or acceptor $A$ molecule. The process is called *resonant* because the excitation and deexcitation processes occur simultaneously without energy dissipation, so that, as first recognized by Förster,[1] perturbation theory can be exploited to calculate the RET probability. Specifically, RET occurs between pairs of molecules that are far enough to neglect the overlap between the orbitals on $D$ and $A$ moieties (Dexter energy transfer is negligible) but whose distance is shorter than the wavelength of the photon needed to excite $A$ or deexcite $D$, so that the radiative energy exchange is irrelevant. In this regime, intermolecular interactions are electrostatic in nature and can be considered as a pertubation on the states of the non-interacting DA system. The Fermi golden rule then gives the RET probability:

$$k_{RET} = \frac{2\pi}{\hbar}|\mathcal{V}_{DA}|^2\delta(\omega_D - \omega_A) \tag{2}$$

where $\mathcal{V}_{DA} = \langle D^*A|H_{int}|DA^*\rangle$ and $\omega_D$ and $\omega_A$ are the frequencies of the $D \rightarrow D^*$ and $A \rightarrow A^*$ processes. RET plays a major role in nature, where among other things, it governs the physics of photosynthesis,[2,3] but also defines the color of the bioluminescence of some jellyfish.[4] Inspired by nature, RET is exploited in artificial photosynthesis,[5,6] in optoelectronic devices,[7,8] and finds extensive application in bioimaging,[9,10] and bioanalysis.[11–13]

The main merit of Förster theory was to express Eq. 2 in terms of experimentally accessible data. The first observation is that RET is typically a slow process if compared with internal relaxation that is usually completed in the first few hundreths of femtosecond

following excitation. It follows that RET occurs from the relaxed D* state, the same state responsible for D fluorescence. Moreover, if intermolecular electrostatic interactions are described in the point dipole approximation, the squared interaction can be written as:

$$|\mathcal{V}_{DA}|^2 = |\frac{1}{4\pi\varepsilon_0\eta^2 r^3}[(\vec{\mu}_D \cdot \vec{\mu}_A) - \frac{3}{r^2}(\vec{\mu}_D \cdot \vec{r})(\vec{\mu}_A \cdot \vec{r})]|^2 = \frac{1}{(4\pi\varepsilon_0)^2}\frac{\kappa^2}{\eta^4 r^6}|\mu_D|^2|\mu_A|^2 \qquad (3)$$

where $\vec{\mu}_{D/A}$ are the transition dipole moments associated with the D fluorescence and A absorption, $\vec{r}$ is the intermolecular distance (vector) and $\eta$ is the medium refractive index. In the second equality, the squared interaction term is factorized into a term that contains (a) the squared amplitude of the two transition dipole moments, that can be estimated from the integrated intensity of absorption transitions in the isolated D and A molecule, (b) the intermolecular distance that enters at the sixth power in the denominator and (c) a geometrical factor $\kappa^2$ that only depends on the mutual orientation of the two dipoles and ranges from 0 to 4.[14] Finally, the Dirac-$\delta$ in Eq. 2, ensuring energy conservation, can be approximated as the overlap $J$ between the (normalized) $D$ fluorescence spectrum and the $A$ absorption spectrum, so that the final expression for the RET probability reads:

$$k_{RET} = (\hbar^2 c)^{-1}|\mathcal{V}_{DA}|^2 J \qquad (4)$$

where $J = \int_0^\infty F_D(\tilde{\nu})A_A(\tilde{\nu})d\tilde{\nu}$ is the spectral overlap between the donor absorption spectrum and the acceptor emission spectrum, each normalized to unit area, expressed in cm and $c$ is the speed of light in cm·s$^{-1}$. The RET rate in Eq. 4 can be translated into a RET-efficiency once the velocities of competing processes are known:

$$\Phi_{RET} = \frac{k_{RET}}{k^D_{rad} + k^D_{nr} + k_{RET}} \qquad (5)$$

where $k^D_{rad}$ and $k^D_{nr}$ are the probability of D* radiative and non-radiative decay, respectively.

Eq. 4 relates the RET rate to the geometry of the RET pair and to experimentally

accessible quantities, opening the way to exploit RET as a *molecular ruler*. The price to be paid is the description of intermolecular electrostatic interactions in the point-dipole approximation, a crude approach for large molecules at short distances, as extensively discussed in recent literature.[15–18] In this respect, more sophisticated approaches have been proposed exploiting transition point-charges,[18] transition cube electron densities[19] or transition density matrices,[20] with further control on the accuracy of $\mathcal{V}_{DA}$ depending on the level of theory.[21]

A delicate issue arises in systems where the geometry of the RET pair is not known or not constrained. In these situations $\kappa^2$ is typically averaged assuming an isotropic distribution of D and A orientations. Two estimates of $\kappa^2$ are adopted in the static and dynamic regimes, corresponding to the two limiting cases where the mutual orientation of the pairs has a very slow or very fast dynamics with respect to the intrinsic RET dynamics.[14] However, the factorization of the distance $r$ and of a orientational factor $\kappa^2$ is not always accurate,[22] and, more generally, closed expressions for $\kappa^2$ are not available for systems in constrained geometry. Some of these issues have been dealt with MD, to calculate average $\kappa^2$ values when closed analytical expressions for the orientational averages are not possible.[22–25]

There is also an additional important factor involving the interplay between RET dynamics and the dynamics of the chromophoric units and their environment. Indeed $\mathcal{V}_{DA}$, depending on the intermolecular distance and on the mutual orientation of the two chromophores, is strongly affected by the dynamics of the system, that, depending on specific conditions, may occur on comparable timescales as RET, leading to a complex interplay of different decay pathways.[26–28] Here, we exploit molecular dynamics (MD) numerical simulations to describe the dynamics of the system at hand. The intermolecular interactions, $\mathcal{V}_{DA}$, is calculated in the point dipole approximation, using the transition dipole moments obtained from quantum chemical calculations on the isolated D and A species. Following the MD trajectories, $\mathcal{V}_{DA}$ acquires therefore a precise time-dependence that is explicitly accounted for in the calculation of the system dynamics. The dynamical treatment of RET is similar to the approach recently proposed by Hoefling et al.,[29,30] but our study allows to

make a direct connection, through MD, between results of quantum chemical calculations and RET dynamics and efficiency for a DA pair in solution.

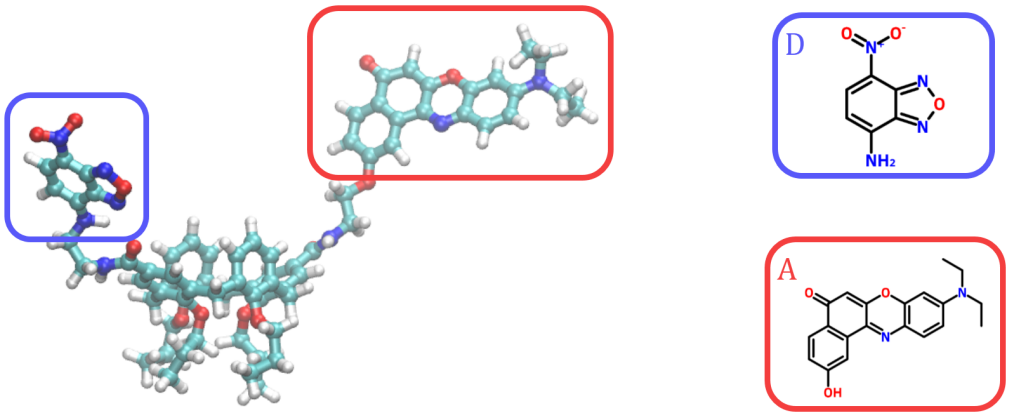


Figure 1: Left: D-clx-A structure; the donor and acceptor are highlighted respectively in blue and red blocks. Right: chromophoric unit structures: 7-nitrobenz-2-oxa-1,3-diazol-4-yl (NBD) and Nile Red (NR).

We consider a supramolecular system where the energy donor, 7-nitrobenz-2-oxa-1,3-diazol-4-yl (NBD), is loosely bound to the energy acceptor, Nile Red (NR), through the flexible bridge offered by a calixarene structure (clx), as in Fig. 1. For this system, a large amount of experimental data collected in different solvents is available.[31] Specifically, the RET dynamics evolves on a wide temporal window ranging from 1 ps to a few ns. Attempts to relate the different timescales to $\mathcal{V}_{DA}$ obtained via TD-DFT for different configurations of the system were unsuccessful, with theoretically estimated timescales ranging from a few tenths to a few hundreds fs.[31] Here, while adopting the same approach to the $\mathcal{V}_{DA}$ estimate, we are able to properly simulate RET timescales thanks to our fully dynamical approach to RET. We will demonstrate that the RET process is governed by a complex interplay between different competing dynamical processes that include not just the D radiative and non-radiative relaxation, but also the conformational and solvation degrees of freedom of the system that, modulating $\mathcal{V}_{DA}$ on similar timescales as RET, cannot be neglected in the

description of this dynamical phenomenon.

In the next section we will shortly describe the proposed dynamical approach to RET that combines an extensive use of MD with TD-DFT estimates of transition dipole moments to calculate time-dependent RET probabilities. This information is then fed into a kinetic model for RET. Results are then shown for the chosen $DA$ pair in two different solvents. In the last section, we will discuss obtained results against available experimental data, showing that the dynamics of the system largely affects observed lifetimes and RET efficiencies, with effects that cannot be recovered via a simple statistical average over different initial configurations.

## 2 Theoretical and computational approach

We present here the multiscale scheme adopted for this work. It can be structured in four steps and it combines MD simulations, excited state calculations and a kinetic coarse-grain model (Fig. 2.).

First, we investigate our reference system NBD-clx-NR (Fig. 1) in chloroform and DMSO. As illustrated in Fig. 2, our procedure starts from a classical MD of the ground state (GS) for the $D$-clx-$A$ system (**step 1**). Simulations were performed with GROMACS package[32] using generalized Amber force field (GAFF[33]) and restrained electrostatic potential atomic partial (RESP[34]) charges. A two-step equilibration phase (1 ns NPT plus 10 ns NVT) is followed by a long (1 $\mu$s) production run in the NVT ensemble. For the production runs a velocity Verlet integrator with all-bond constraint and a simulation timestep of 0.5 fs is employed, combined with a velocity-rescale thermostat coupled via a $\tau_T$=0.1 ps.[35] (more information in section S1.1 and S1.2). This long GS trajectory simulates the statistical distribution of the system configurations at equilibrium (step 1 in Figure 2). DMSO and chloroform solvents were also consistently described by GAFF force field, which has been shown to correctly predict many properties of bulk solvents.[36]

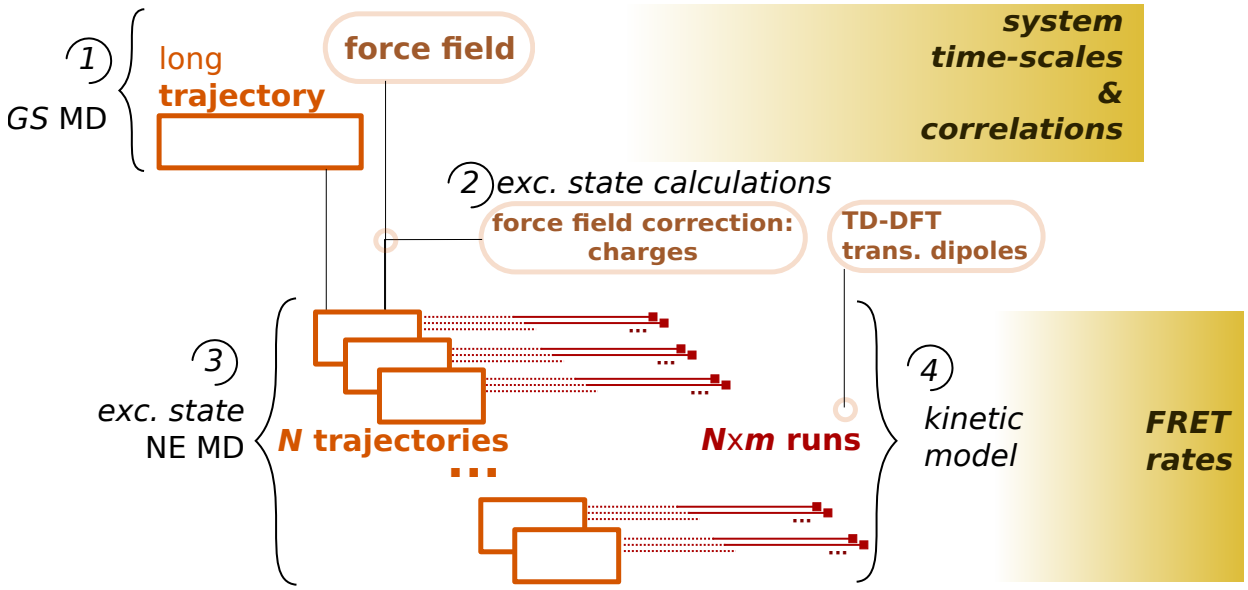


Figure 2: A sketch of the 4-step multiscale model used for this work. See text for a detailed description of step 1-4.

Excited-state calculations were performed on isolated (gas phase) $D$ and $A$ species **(step 2)** to determine i) excited state charges for $D$ at HF-CIS, 6-31G(d,p) basis set and ii) transition dipole moments at TD-DFT with B3LYP functional and 6-31G(d,p) basis set for $D$ and $A$. TD-DFT gas phase transition energies are overestimated with respect to experiment (see Table 1), as expected due to solvation effects, and in any case are consistent with the adopted GAFF approach. Further details about TD-DFT results, including solvation effects can be found in Sect. S1.3. $D$ excitation is simulated by instantaneously switching the molecular force field and geometry from those relevant to $D$ to those relevant to $D^*$ (see S1.4). To account for the excitation of a statistically relevant distribution of $D$ molecules in solution, the GS trajectory is sampled to generate $N$ non-equilibrium (NE) trajectories of $D^*A$ (**step 3**), each trajectory starting upon instantaneous excitation of the $D$ molecule. In our NE MD we neglect the molecular geometry relaxations when switching to the excited state. Moreover, the choice of the velocity-rescale thermostat with a coupling value around $\tau_T \sim 10^{-1}$ ps and a very short timestep (0.5 fs) properly simulate fluctuations and dynamical properties as relevant to the NVE ensemble,[35] giving us confidence on the quality of our NE MD simulations.

Along each NE trajectory, the t-dependence of $\mathcal{V}_{DA}$ is then calculated according to Eq. 3, setting $\eta = 1.45$, and using the transition dipole moments $\mu_A$ and $\mu_D$ obtained form TD-DFT in step 2. Specifically, $\mu_A$ and $\mu_D$ are obtained from TD-DFT calculation (B3LYP 6-31g(d,p) (see S1.3) and their magnitude is maintained constant during the simulation, while their orientation is anchored to the chromophore plane (see S1.5). The $t$-dependence of $\mathcal{V}_{DA}$ is therefore only due to the relative motion of the two molecular sub-units. We then exploit Eq. 4 to calculate the $t$-dependent RET-probability $k_{RET}(t)$, setting $J_{CHCl_3} = 1.95 \cdot 10^{-4}$ cm and $J_{DMSO} = 1.77 \cdot 10^{-4}$ cm, as obtained from the overlap of the experimental emission profile for $D$ and absorption profile for $A$.[31]

Table 1: TD-DFT absorption and emission energies and squared transition dipole moments relevant to the lowest excited state of NBD ($D$) and NR ($A$) in the gas phase (emission energy refers to relaxed excited state geometry) and corresponding experimental transition energies.[31]

| | **NBD absorption** | **NR emission** |
|---|---|---|
| Exp. trans. energies (eV)[31] | 2.38 | 2.30 |
| TD-DFT B3LYP trans. energies (eV) | 2.75 | 2.71 |
| TD-DFT B3LYP $\mu_t^2$ (Debye$^2$) | 1.50 | 9.55 |

Having obtained $N$ independent and statistically representative profiles for the $\mathcal{V}_{DA}(t)$ and $k_{RET}(t)$ dependence, we are now in the position to address the system relaxation as governed by the interplay between the radiative and non radiative decay of $D^*$ and RET through our stochastic kinetic model (**step 4**), inspired to kinetic Monte Carlo. Much as with the transition dipole moments, we assume that the radiative and non-radiative decay rates of $D^*$, $k_r$ and $k_{nr}$ respectively, are molecular properties and are therefore barely affected by the dynamics. These quantities are experimentally accessible through the fluorescence lifetime $\tau_{fl}$:

$$\frac{1}{\tau_{fl}} = k_r + k_{nr} \tag{6}$$

It is of course possible to separate radiative and nonradiative decay rates exploiting the experimental fluorescence quantum yield,[14] but RET efficiency is governed by the competition

between RET and the overall decay of $D$, making the discrimination between radiative and non-radiative decay irrelevant. For $\tau_{fl}$ of $D$ we use the experimental values of 7 and 9 ns in chloroform and DMSO solutions, respectively.[31]

For each one of the $N$ NE trajectories (step 3) we then have constant $k_r + k_{nr}$ and time-dependent $k_{RET}(t)$ defining (for a given time and trajectory) the probability of the concurrent D-relaxation pathways. At each timestep this global decay probability is compared with a random number to decide the fate of the system that may either stay unaffacted or decay (either by a radiative or non-radiative process, or undergo RET). Of course each of such *kinetic-model run* (decay simulation) will stop as soon as $D^*A$ decays following any of the possible channels, defining in this way a decay time. Additional technical details may be found in Sect. S1.6 of the S.I.. To improve the statistical significance of the results, $m$ independent stochastic decay simulations are run on each one of the $N$ independent NE trajectories. By collecting results obtained for the $N \times m$ decay runs, a time-dependent profile of the $D^*$ population is finally obtained.

# 3 Results and Discussions

## 3.1 Ground state dynamics

Extensive ground state dynamics were run for NBD-clx-NR in chloroform and DMSO up to 1 $\mu$s to ensure that the whole configurational space is explored by the system. A representative and strongly relevant variable for our problem is the distance $d$ between the centers of mass (COM) of the $D$ and $A$ units. The probability distributions from these dynamics can be converted to reconstruct the free energy profiles along $d$, as in Fig. 3. In both solvents, a deep minimum is observed at $d \sim 4$ Å, corresponding to a configuration named "closed/stacked" that maximizes the intermolecular $\pi - \pi$ interactions, as confirmed by a detailed analysis of the correlation between $d$ and the two angles defining the mutual orientation of the chromophores. Specifically, we define $\theta_\mu$ as the angle formed between the dipole moments

on $D$ and $A$ fragments and $\theta_\pi$ as the angle between the two vectors perpendicular to the molecular planes. In the "closed/stacked" configuration indeed $\theta_\mu \sim 0$ and $\theta_\pi \sim \pm 180$ (see section S2 of S.I.). In chloroform, two other minima are observed namely, a "closed/NH" conformation, where a hydrogen bond bridges the $D$ and $A$ molecules, and a "closed/open" conformation where the two dyes are relatively free (wider minimum) and the maximum distance is only constrained by the clx scaffold in closed flattened cone conformation. In DMSO, these two minima observed in chloroform merge into a single very broad minimum denoting the larger conformational flexibility of the system, related most probably to a stronger solute-solvent interaction that weakens intramolecular interactions. This results support the previous analysis,[31] based on experimental NMR data, pointing to a larger weight of *open-flattened conformations* for the clx structure in DMSO, with respect to the *closed-flattened conformations* dominating in chloroform. Our results are also in line with the DFT analysis of stable structures,[31] even if our explicit-solvent MD simulations do not assign a significant population to the open/CH conformer (open flattened clx cone with weak interactions between A and the clx methylene bridge).

To probe the characteristic timescales of the conformational motion we calculate the time-autocorrelation functions associated to the three main geometrical variables characterizing the system, $d$, $\theta_\mu$ and $\theta_\pi$. For each generic variable $A$ the time-autocorrelation function is defined as:

$$C_{AA}(t_k) = \frac{1}{N_s - k} \sum_{j=1}^{N_s - k} A(t_j) A(t_{j+k}) \quad k = 1, 2, 3, \ldots, N_s \tag{7}$$

where $N_s$ is the total number of steps and $t_j = (j-1)\Delta t$, with $\Delta t$ measuring the time step. The results in Fig. 4 confirm a strong similarity of behaviour in chloroform for the intermolecular distance and the orientational motions, with all variables dynamically active on a timescale of $\sim$10 ns. In contrast, in DMSO the orientational motion occurs on a faster timescale ($\sim$ 1 ns) that the variation of intermolecular distances ($\sim$ 5 ns).

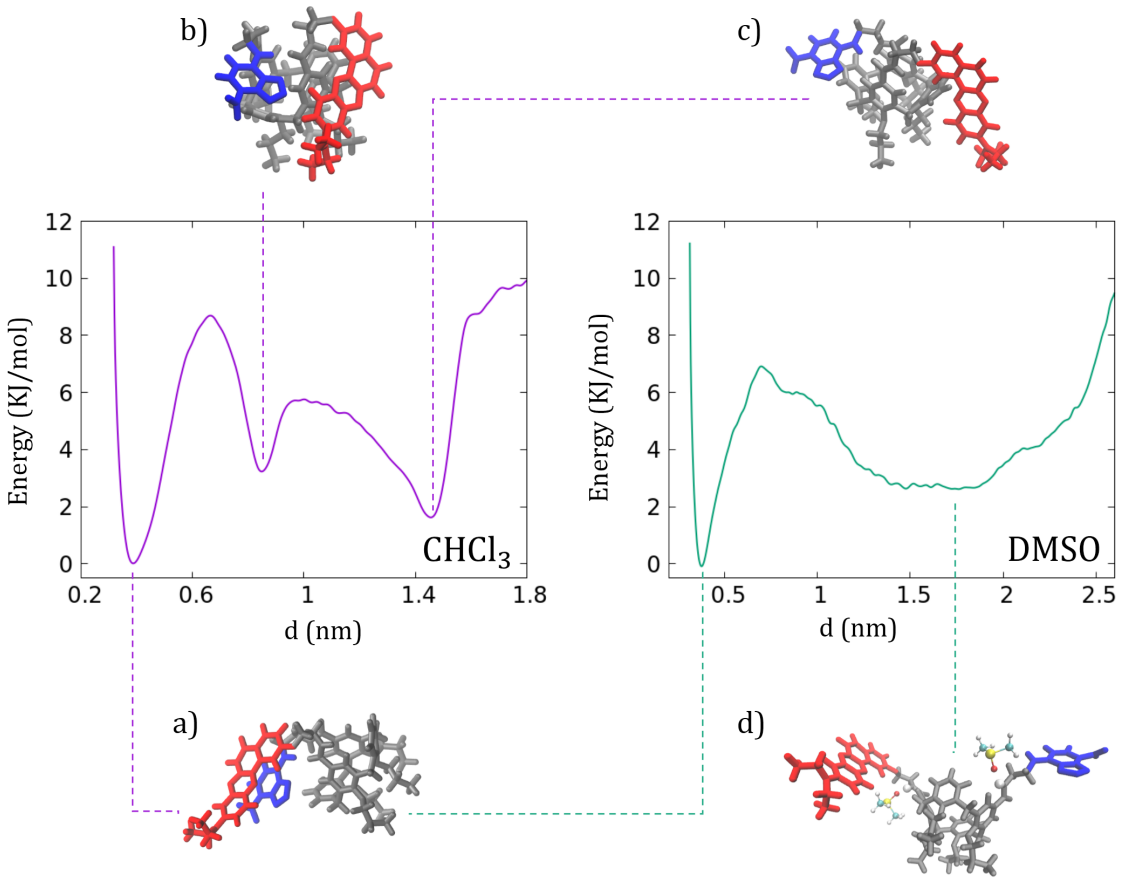


Figure 3: Free energy potential curves constructed against the distance between D and A COM for D-clx-A in chloroform (left) and DMSO (right). Representative structures are shown for each energy minimum in chlorofrom (a,b,c) and DMSO (a,d).

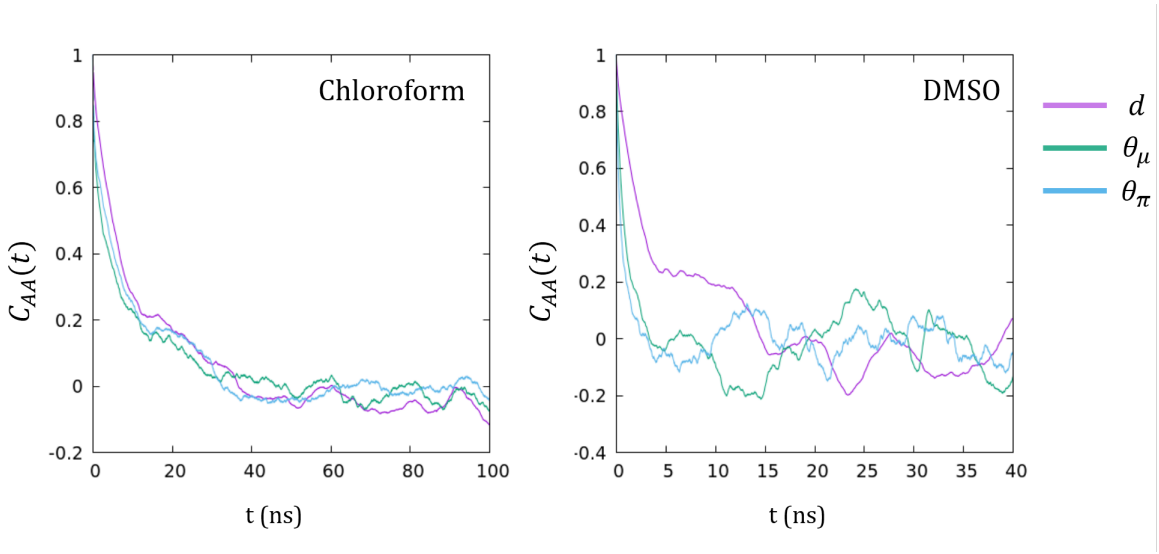


Figure 4: Autocorrelation functions of distance, $\theta_\mu$ and $\theta_\pi$ between D and A for D-clx-A in chloroform (left) and DMSO (right).

## 3.2 Non-equilibrium dynamics and RET

Out of the ground state trajectory, $N$ independent configurations are selected randomly ($N$=1000 and 100 for chloroform and DMSO simulations, respectively) as starting points for the NE dynamics after impulsive $D$ excitation. The most important information to be extracted from the NE trajectories is the time-evolution of $\mathcal{V}_{DA}$. Very different behaviors are observed for $\mathcal{V}_{DA}(t)$ depending on the starting point, as exemplified by the three trajectories in Fig. 5, selected out of the NE trajectories calculated for chloroform solution (analogous examples for DMSO solution are shown in Section S3 of S.I.). Trajectory 1 refers to a system where the dyes stay very close ($d < 0.5$ nm) all along the trajectory. Large $\mathcal{V}_{DA} \sim 300$ cm$^{-1}$ are calculated in this case with sizable oscillations ascribed to the orientational motion of the dyes, that largely modulate the dipole-dipole interactions. In trajectory 2 the dyes are far apart ($d >$1.5 nm) with negligible interactions, except for a couple of short time windows where they come closer, leading to sizable interactions. Finally trajectory 3 starts with the dyes far apart and negligible interactions, but after about 5 ns a configuration is reached where the two dyes are much closer ($d < 0.5$ nm) and the interaction strength becomes sizeable, basically regaining the same regime described by trajectory 1.

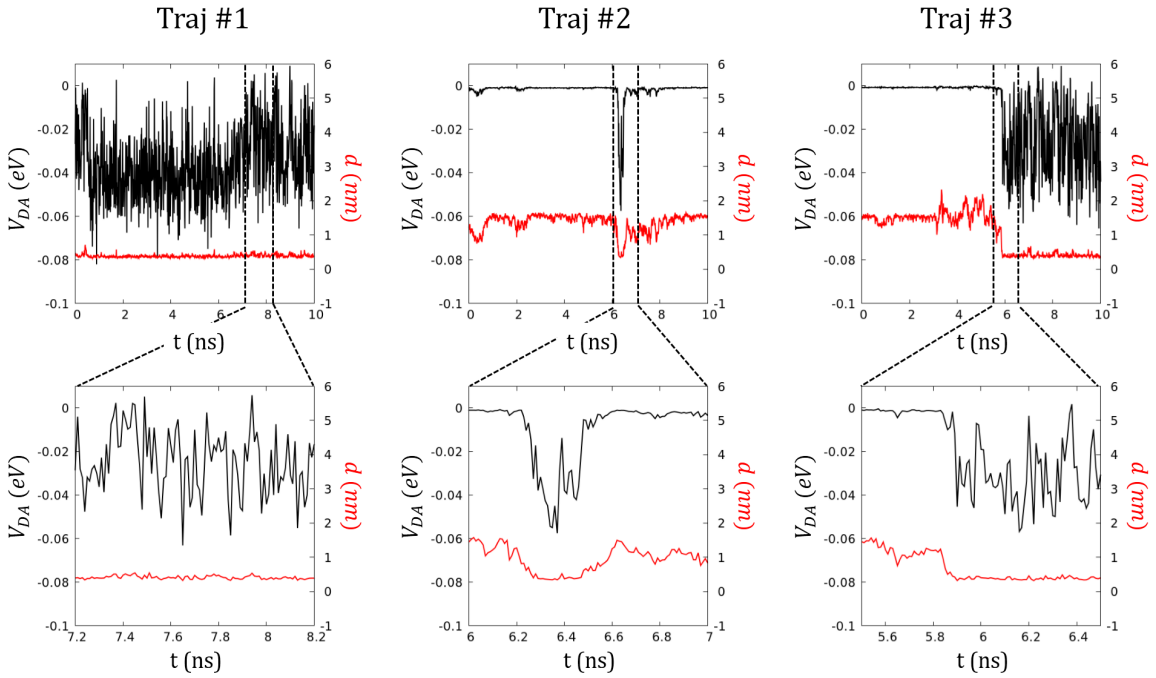


Figure 5: For three selected NE trajectories extracted from the N=1000 calculated in chloroform, we plot the time-dependence profile of the DA interaction energy, $\mathcal{V}_{DA}$, (black) and the distance $d$ between D and A COMs (red). Top panels: full NE trajectory; bottom panels: zoom over a short time-window.

The qualitatively different behavior observed for RET pairs excited at different starting conformations clearly demonstrates the impossibility to reliably predict the RET efficiency of a disordered dynamical system by simply averaging over different conformational and orientational states, as traditionally done when applying Eq. 3 to disordered systems using an average $\kappa^2$ value. To overcome this problem, we exploit the kinetic approach outlined in Section 2: having obtained $N$ time-dependent profiles for $\mathcal{V}_{DA}$ and hence for $\kappa_{RET}$ (one for each NE trajectory), we perform for each trajectory $m$ independent kinetic runs. Following the information (i.e. the deactivation times) obtained from the resulting $m \times N$ kinetic replicas, we obtain the time-dependence of the population of $D^*$ state as well as the RET efficiency, calculated as the ratio of the RET events over the total RET and relaxation events.

Fig. 6 shows the time-dependence of the $D^*A$ population and collects our main results. Dashed lines show the simple exponential decay of the isolated $D^*$ species. The existence of the RET channel obviously leads to a faster depopulation of the excited D and to a more complex behavior that does not fit a single exponential. To further investigate the role of dynamic degrees of freedom, for comparison purposes, we also performed *static* simulations where the decay is calculated maintaining $\mathcal{V}_{DA}$ constant to the value obtained at the initial instant of each NE dynamics. Comparing the calculated $D^*A$ relaxation obtained from the fully dynamic calculation (black lines) vs the static calculation (red lines) is instructive. It clearly shows that the conformational motion occurring after the excitation affects the interactions in the RET pair and hence RET probabilities. The conformational motion, occuring on comparable timescales as RET itself, strongly affects the relaxation dynamics of the system. Specifically, RET is much faster in a fully dynamical calculation than in a static approach. This can be easily understood: in the dynamical calculation in fact, the system explores a wide conformational space - including regions with fast RET decay. When these "hot spots" are reached, they offer preferential channels for relaxation.[26–28] In a static simulation, once the population of these hot spots is depleted, they become ineffective and RET necessarily occurs along slower channels. On the contrary, in a dynamical model, the

population is continuously transferred to replenish these hot spots, so that fast channels stay active all along the process. Quite interestingly, the different results obtained in the static and dynamic calculations cannot be ascribed to different distributions of $\mathcal{V}_{DA}$. Indeed the $\mathcal{V}_{DA}$ histograms calculated along the static and dynamic trajectories shown in Fig. 6 are very similar. As the static scenario only refers to a sampling through GS MD, while the dynamic one is the results of the excited state (namely NE) dynamics, the similarity of the two distributions suggests that the sources of non-equilibrium effects are actually rather modest.

Overall MD simulations are crucial in order (i) to obtain a proper description of the $\mathcal{V}_{DA}$ distribution, not relying on a preselected set of conformations and (ii) to assess the dynamical behavior of $\mathcal{V}_{DA}$ and hence to account for the competition of the different decay pathways, fully accounting for the conformational dynamics of the system and its effect on the instantaneous RET probabilities.

For a quantitative analysis, we fitted the RET decay curves with multiple exponentials, veryfing their statistical significance. We fitted the full-dynamical result for chloroform solution with 4 exponentials with relaxation times: 1.8, 56, 313 and 1035 ps. The static calculation cannot reproduce the very fast initial relaxation and only three relaxation times fit the red curve in fig. 6: 9.8, 134 and 853 ps. The deviation of static results from the fully dynamic calculations are even larger in DMSO, where the dynamic calculation has 4 exponential with relaxation times 7.4, 33, 546 and 2075 ps, while the static result can be fit with three relaxation times: 9.64, 765, 3309 ps (more details about the analysis are reported in section S4 of S.I.).

The different RET dynamics corresponds quite naturally to different RET quantum yield that are estimated form the fully dynamical calculation as 0.96 and 0.88 for chloroform and DMSO solutions, respectively, and reduce to 0.94 and 0.69 in the static calculation. The faster and more efficient RET in chloroform solutions, if compared with DMSO solution can be ascribed to the slower conformational dynamics of the RET pair in chloroform than in

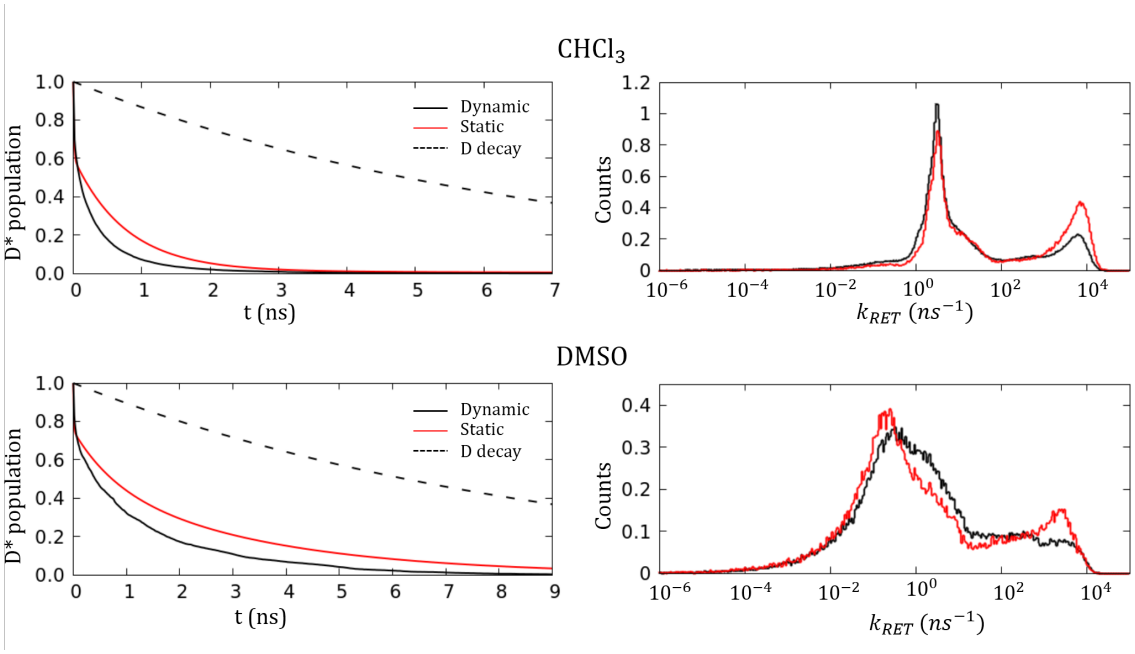


Figure 6: Left panels: decay of the D* population calculated in chloroform (top) and DMSO (bottom). Dashed lines refer to the exponential decay of the isolated D species; the red lines show static results (obtained neglecting the conformational motion of the excited RET pair after excitation), the black lines show the full dynamical result. Right panels show the (area normalized) distributions of RET rates, resulting from a static and dynamic calculations for both solvents.

DMSO (see Fig. 4) that brings it precisely in the time-scale of relevance to RET.

Our results are in very good agreement with experiment: three different exponentials were extracted from experimental data,[31] that amount to 2, 17 and 1800 ps in chloroform solution, and to 4.0, 59 and 4500 ps in DMSO. Quite interestingly, our results solve an issue left open by the theoretical analysis that accompanied the experimental work. In that work,[31] looking just at the two most probable configurations, the authors estimated $\mathcal{V}_{DA}$ of the same order of magnitude as we estimate in our work. Translating these interaction strengths directly into RET probability, estimated lifetimes turned out in the 0.03-0.35 ps range, at least one order of magnitude smaller than the smallest experimental time, and several orders of magnitude smaller than the largest experimental lifetime. A complete MD dynamics, allowing our flexible system to explore a large configuration space, is needed to get sense of the experimentally observed relaxation times.

# 4 Conclusion

A multiscale computational protocol is proposed for the calculation of the RET dynamics and quantum yields for a solvated donor-acceptor pair highlighting the importance of conformational fluctuations. The proposed approach is validated against an extensive set of experimental results available for a RET-pair bound via flexible links to a calixarene scaffold. The comparison with the experiment is very good and indeed solves a theoretical problem associated with this system, where estimates of $\mathcal{V}_{DA}$ from TD-DFT calculations on few preselected representative configurations of the D-clx-A system, underestimated the RET lifetimes by several orders of magnitude.[31]

Our approach combines equilibrium and non-equilibrium MD calculations with TD-DFT results, leading to a detailed description of the concurrent processes: $D^*$ decay, energy transfer and conformational dynamics. The conformational motion modulates $\mathcal{V}_{DA}$, the intermolecular interaction responsible for RET. In a fully dynamical picture the system af-

ter photoexcitation is allowed to explore conformational regions where $\mathcal{V}_{DA}$ is large, then opening fast RET channels and leading to faster RET than in a static picture, where the conformational motion is frozen.

RET in disordered systems is a delicate issue: the standard approach relying on the use of an average $\kappa^2$ value has been questioned in several ways. In the first place the factorization of the $\mathcal{V}_{DA}$ interaction in a term $\kappa^2$ that only depends on the intermolecular orientation and in a term that only depends on the intermolecular distance, is incorrect - particularly if the system can explore regions where intermolecular distances are comparatively short. More generally those approaches represent a too crude approximation to describe $DA$ interactions in systems, like the one investigated here, where a complex supramolecular structure poses serious constraints to the mutual arrangements of the $D$ and $A$ moieties. We show that these problems can be easily addressed by ground state MD calculations, that offer reliable information on the conformational heterogeneity of the RET pair. However, we also demonstrated that this is not sufficient in the case investigated here. In such flexible systems, the conformational motion modulates intermolecular interactions on a timescale relevant to RET, leading to important effects that cannot be accounted for through an orientational average in either in the static or ultrafast regime.

## Supporting Information Available

Further computational details, Conformational analysis, NE trajectories, Exponential fitting parameters, List of RESP atomic charges.

## References


(1) Förster, T. Zwischenmolekulare Energiewanderung und Fluoreszenz. *Ann. Phys.* **1948**, *437*, 55–75.

(2) Scholes, G. D.; Harcourt, R. D.; Fleming, G. R. Electronic Interactions in Photosynthetic Light-Harvesting Complexes: The Role of Carotenoids. *J. Phys. Chem. B* **1997**, *101*, 7302–7312.

(3) Wu, E. C.; Arsenault, E. A.; Bhattacharyya, P.; Lewis, N. H. C.; Fleming, G. R. Two-dimensional electronic vibrational spectroscopy and ultrafast excitonic and vibronic photosynthetic energy transfer. *Faraday Discuss.* **2019**, *216*, 116–132.

(4) Morise, H.; Shimomura, O.; Johnson, F. H.; Winant, J. Intermolecular Energy Transfer in the Bioluminescent System of Aequorea. *Biochemistry* **1974**, *13*, 2656–2662, PMID: 4151620.

(5) Ragni, R.; Leone, G.; Rizzo, G.; la Gatta, S.; Milano, F.; Trotta, M.; Farinola, G. M. Synthesis of two cyanine dyes as potential artificial antennas for the bacterial photosynthetic Reaction Center. *MRS Advances* **2019**, *4*, 1293–1298.

(6) Zhang, B.; Sun, L. Artificial photosynthesis: opportunities and challenges of molecular catalysts. *Chem. Soc. Rev.* **2019**, *48*, 2216–2264.

(7) Xu, T.; Yang, M.; Liu, J.; Wu, X.; Murtaza, I.; He, G.; Meng, H. Wide color-range tunable and low roll-off fluorescent organic light emitting devices based on double undoped ultrathin emitters. *Org. Electron.* **2016**, *37*, 93 – 99.

(8) Lyskov, I.; Etinski, M.; Marian, C. M.; Russo, S. P. Exciton energy transfer in organic light emitting diodes with thermally activated delayed fluorescence dopants. *J. Mater. Chem. C* **2018**, *6*, 6860–6868.

(9) Arai, Y.; Nagai, T. Extensive use of FRET in biological imaging. *Microscopy* **2013**, *62*, 419–428.

(10) Morla-Folch, J.; Vargas-Nadal, G.; Zhao, T.; Sissa, C.; Ardizzone, A.; Kurhuzenkau, S.; Köber, M.; Uddin, M.; Painelli, A.; Veciana, J.; Belfield, K. D.; Ventosa, N. Dye-Loaded Quatsomes Exhibiting FRET as Nanoprobes for Bioimaging. *ACS Appl. Mater. Interfaces* **2020**,

(11) Szöllosi, J.; Damjanovich, S.; Mátyus, L. Application of Fluorescence Resonance Energy Transfer in the Clinical Laboratory: Routine and Research. *Cytometry* **1998**, *34*, 159–179.

(12) Miller, J. N. Fluorescence energy transfer methods in bioanalysis. *Analyst* **2005**, *130*, 265–270.

(13) Lu, H.-J.; Xu, J.-J.; Zhou, H.; Chen, H.-Y. Recent advances in electrochemiluminescence resonance energy transfer for bioanalysis: Fundamentals and applications. *TrAC, Trends Anal. Chem.* **2020**, *122*, 115746.

(14) Lakowicz, J. R. *Principles of Fluorescence Spectroscopy*, 3rd ed.; Springer US, 2006.

(15) Wong, K. F.; Bagchi, B.; Rossky, P. J. Distance and Orientation Dependence of Excitation Transfer Rates in Conjugated Systems: Beyond the Förster Theory. *J. Phys. Chem. A* **2004**, *108*, 5752–5763.

(16) Scholes, G. D.; Jordanides, X. J.; Fleming, G. R. Adapting the FÖRster Theory of Energy Transfer for Modeling Dynamics in Aggregated Molecular Assemblies. *J. Phys. Chem. B* **2001**, *105*, 1640–1651.

(17) Beljonne, D.; Curutchet, C.; Scholes, G. D.; Silbey, R. J. Beyond FoÖRster Resonance Energy Transfer in Biological and Nanoscale Systems FÖRster Resonance Energy Transfer in Biological and Nanoscale Systems. *J. Phys. Chem. B* **2009**, *113*, 6583–6599.

(18) Sissa, C.; Manna, A. K.; Terenziani, F.; Painelli, A.; Pati, S. K. Beyond the Förster formulation for resonance energy transfer: the role of dark states. *Phys. Chem. Chem. Phys.* **2011**, *13*, 12734–12744.

(19) Krueger, B. P.; Scholes, G. D.; Fleming, G. R. Calculation of Couplings and Energy-Transfer Pathways between the Pigments of LH2 by the *Ab Initio* Transition Density Cube Method. *The J. Phys. Chem. B* **1998**, *102*, 5378–5386.

(20) Voityuk, A. A. Fragment Transition Density Method to Calculate Electronic Coupling for Excitation Energy Transfer. *The J. Chem. Phys.* **2014**, *140*, 244117.

(21) You, Z.-Q.; Hsu, C.-P. Theory and Calculation for the Electronic Coupling in Excitation Energy Transfer. *Int. J. Quantum Chem.* **2014**, *114*, 102–115.

(22) Shoura, M. J.; Ranatunga, R. J.; Harris, S. A.; Nielsen, S. O.; Levene, S. D. Contribution of Fluorophore Dynamics and Solvation to Resonant Energy Transfer in Protein-DNA Complexes: A Molecular-Dynamics Study. *Biophys. J.* **2014**, *107*, 700–710.

(23) Calero, S.; Lago, S.; Garzón, B. Classical Molecular Dynamics Simulation of Kappa Squared Factor in Resonance Energy Transfer for Linear Dipole Models. *Molecular Simulation* **2003**, *29*, 519–525.

(24) Urzúa-Leiva, R. A.; Rampino, S.; Arratia-Perez, R.; Mosconi, E.; Pastore, M.; Angelis, F. D. Thermal Fluctuations on FÖRster Resonance Energy Transfer in Dyadic Solar Cell Sensitizers: A Combined *Ab Initio* Molecular Dynamics and TDDFT Investigation. *J. Phys. Chem. C* **2015**, *119*, 16490–16499.

(25) Reinartz, I.; Sinner, C.; Nettels, D.; Stucki-Buchli, B.; Stockmar, F.; Panek, P. T.; Jacob, C. R.; Nienhaus, G. U.; Schuler, B.; Schug, A. Simulation of FRET Dyes Allows Quantitative Comparison against Experimental Data. *J. Chem. Phys.* **2018**, *148*.

(26) Stryer, L.; Thomas, D. D.; Meares, C. F. Diffusion-Enhanced Fluorescence Energy Transfer. *Annual Review of Biophysics and Bioengineering* **1982**, *11*, 203–222.

(27) Wallace, B.; Atzberger, P. J. Förster Resonance Energy Transfer: Role of Diffusion of Fluorophore Orientation and Separation in Observed Shifts of FRET Efficiency. *PLOS ONE* **2017**, *12*, e0177122.

(28) Di Maiolo, F.; Painelli, A. Dynamical disorder and resonance energy transfer: a novel quantum-classical approach. *Phys. Chem. Chem. Phys.* **2020**, *22*, 1061–1068.

(29) Hoefling, M.; Lima, N.; Haenni, D.; Seidel, C. A.; Schuler, B.; Grubmüller, H. Structural Heterogeneity and Quantitative FRET Efficiency Distributions of Polyprolines through a Hybrid Atomistic Simulation and Monte Carlo Approach. *PLoS ONE* **2011**, *6*.

(30) Hoefling, M.; Grubmüller, H. In Silico FRET from Simulated Dye Dynamics. *Comput. Phys. Commun.* **2013**, *184*, 841–852.

(31) Tosi, I.; SegadoCentellas, M.; Campioli, E.; Iagatti, A.; Lapini, A.; Sissa, C.; Baldini, L.; Cappelli, C.; DiDonato, M.; Sansone, F.; Santoro, F.; Terenziani, F. Excitation Dynamics in Hetero-Bichromophoric Calixarene Systems. *ChemPhysChem* **2016**, *17*, 1686–1706.

(32) Abraham, M. J.; Murtola, T.; Schulz, R.; Páll, S.; Smith, J. C.; Hess, B.; Lindahl, E. GROMACS: High performance molecular simulations through multi-level parallelism from laptops to supercomputers. *SoftwareX* **2015**, *1-2*, 19 – 25.

(33) Wang, J.; Wolf, R. M.; Caldwell, J. W.; Kollman, P. A.; Case, D. A. Development and Testing of a General Amber Force Field. *J. Comput. Chem.* **2004**, *25*, 1157–1174.

(34) Bayly, C. I.; Cieplak, P.; Cornell, W.; Kollman, P. A. A Well-Behaved Electrostatic Potential Based Method Using Charge Restraints for Deriving Atomic Charges: the RESP Model. *J. Phys. Chem.* **1993**, *97*, 10269–10280.

(35) Bussi, G.; Donadio, D.; Parrinello, M. Canonical sampling through velocity rescaling. *J. Chem. Phys.* **2007**, *126*, 014101.

(36) Caleman, C.; van Maaren, P. J.; Hong, M.; Hub, J. S.; Costa, L. T.; van der Spoel, D. Force field benchmark of organic liquids: density, enthalpy of vaporization, heat capacities, surface tension, isothermal compressibility, volumetric expansion coefficient, and dielectric constant. *J. Chem. Theory Comput.* **2012**, *8*, 61–74.

# Graphical TOC Entry